Journal of Materials Chemistry A

Accepted Manuscript

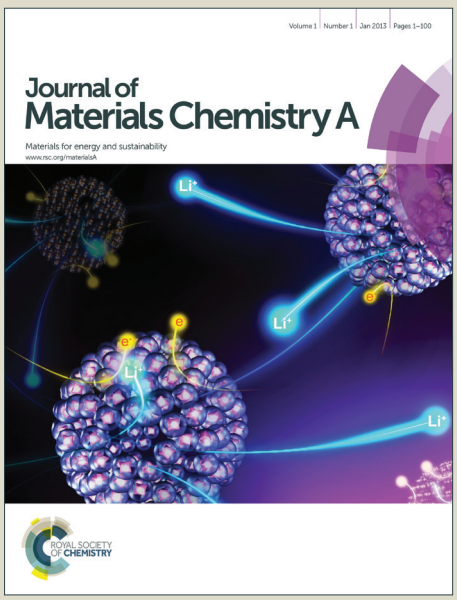

ROYAL SOCIETY OF CHEMISTRY

www.rsc.org/materialsA

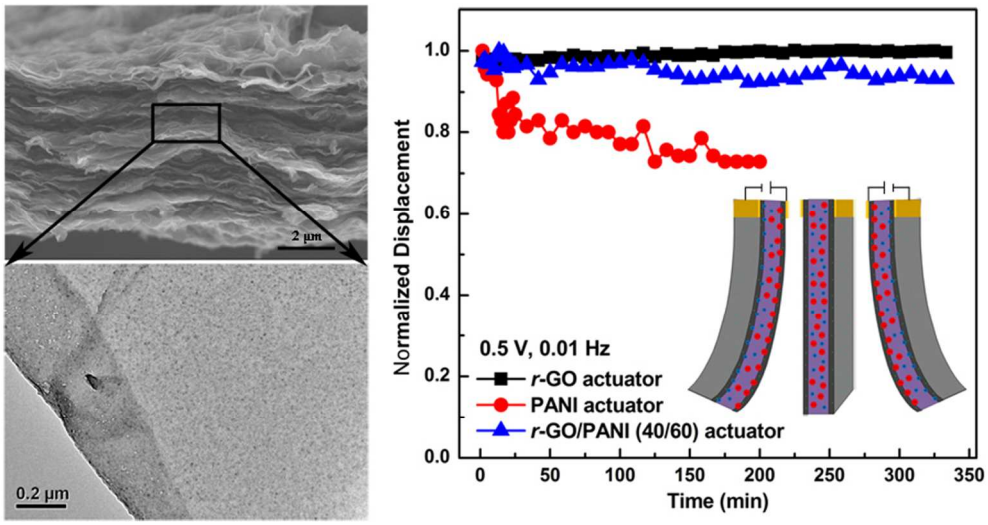

76x39mm (300 x 300 DPI)

r-GO/PANI nanocomposite based air working ionic actuator demonstrates large actuation stroke and long-term durability.

Journal of Materials Chemistry A

Dynamic Article Links ►

Cite this: DOI: 10.1039/c0xx00000x

ARTICLE TYPE

www.rsc.org/xxxxxx

Synergistic Effect of *r*-GO/PANI Nanocomposite Electrode based Air Working Ionic Actuator with Large Actuation Stroke and Long-Term Durability

Qing Liu[a, b], Luqi Liu[*, a], Ke Xie[a], Yuena Meng[a, b], Haiping Wu[a, b], Guorui Wang[a], Zhaohe Dai[a, b], Zhixiang Wei[a], Zhong Zhang[*, a]

Received (in XXX, XXX) Xth XXXXXXXXX 20XX, Accepted Xth XXXXXXXXX 20XX
DOI: 10.1039/b000000x

Actuators can directly convert various types of energy into mechanical motions. In this work, we constructed a novel air working ionic actuator by sandwiched sulfuric acid-poly (vinyl alcohol) (H_2SO_4-PVA) gel electrolyte and two pieces of reduced graphene oxide/polyaniline (*r*-GO/PANI) nanocomposite film based electrodes, in which the PANI nanoparticles were uniformly decorated onto *r*-GO sheets surface through in situ polymerization method. Combination of supra mechanical, electrical conductivity, large surface area of individual graphene sheet and excellent electrochemical property of PANI component makes the composite electrodes with good mechanical and high electrochemical capacitance. Later tests indicated that actuator could be stimulated under low driving voltage (≤ 0.5 V) without trade-off actuator strokes, and behaved excellent long-term actuation durability. Under a 0.5 V operating voltage, the actuation strain of *r*-GO/PANI actuator could reach 0.327%, corresponding to a 30 MPa generated stress. We attribute the excellent actuation performances to the synergistic effect of *r*-GO sheets and PANI component.

Introduction

Actuators that can directly convert various energies to mechanical energy have shown great potential in many fields such as artificial muscles, robots and sensors, etc.[1-5] Among all the electrically stimulated actuators that have been explored, air operable ionic actuators have been extensively studied in recent decades for their impressive actuation performances under relatively lower driving voltage.[6-8] Generally, the air working ionic actuator is constructed of an ionic conductive electrolyte layer laminated by two pieces of electrically conductive electrode membranes. During actuation process, ions migration caused by the applied electric field induces volume difference of the anode and cathode layers, and the actuator strip will bend forth and back under an alternative potential. Even though traditional ionic polymer-metal composite (IPMC) type actuators have been commercially available in recent years, the intrinsic weaknesses of metal electrode layers (*e. g.* silver, gold, and platinum), including low flexibility, cracking of metal electrodes during the application process, and high manufacturing cost, have greatly limited their wide applications in smart material fields.[6, 9] Thus, it is a great challenge to explore novel electrode materials with higher flexibility and excellent electromechanical stability for next-generation of air working ionic actuators.

Nanostructured carbon materials such as one-dimensional (1D) carbon nanotubes (CNT) and two-dimensional (2D) graphene have attracted extensive attention in smart material fields due to their excellent electrical conductivities, outstanding mechanical properties, large specific surface area and thermal/chemical stability.[10, 11] Baughman firstly reported a single wall carbon nanotubes (SWCNT) based ionic actuator that could work in an electrolyte solution, demonstrated the potential applications of nanostructured carbon materials in ionic actuators.[12] Since then, CNT has been explored to satisfy various requirements of ionic actuator electrodes, and plenty of works have proved the excellent actuation performances of CNT electrode based air working actuators. For instance, Aida *et al*. have proved the excellent electromechanical stability of the CNT gel based actuator, and only a 20% decrease in the actuator stroke was observed after 15 hours actuation.[8] It should be noted, however, that the force generation was limited due to the low modulus of the gel electrodes.[13]

Having intrinsically structural similarity for both CNT and graphene building blocks, graphene based paper materials show higher tensile mechanical properties compared to CNT Bucky paper.[11] Thus, the enhancements in output stress and power density are expected once graphene papers are utilized as actuator electrodes. Experimentally, different from CNT prepared by chemical vapour deposition (CVD) method, graphene sheets could be easily prepared on large scale by chemical reduction of graphene oxide (GO), which would extremely facilitate the electrode fabrication.[14, 15] Theoretical calculations have predicted

that the quantum-mechanical strain of graphene in basal plane direction could reach 0.2 % while the electrostatic double-layer strain could reach 1 % for charge injection, which are much higher than that of CNT.[16, 17] Therefore, ionic actuators with large actuation strokes and high generated stress would be obtained once graphene papers are utilized as electrodes. Previous works have demonstrated the potential applications of graphene film based electrode in liquid-type ionic actuators [18, 19] It is worth noting, however, that the densely stacking nature of graphene sheets hinders the ion migration, and severely deteriorates the actuation performance of graphene based ionic actuators, particularly in air condition. Thus, it is crucially important to design graphene based electrodes with loosely packed architectures, which could exhibit large actuation strokes, high stress generation, and good stability.

Earlier works have proved that, incorporating a second component, such as CNT or nanoparticles, was a promising approach to prevent restacking of graphene sheets.[20-23] For instance, the incorporated CNT could greatly restrain the restacking behaviour of individual graphene or GO sheets, and facilitate the diffusion of electrolytes across electrode layers. Consequently, the improvement in both electrochemical and actuation properties were obtained in graphene/CNT hybrid electrodes based actuators.[21, 22] Chen *et al.* reported that, under a 2 V, 0.01 Hz square wave potential, the actuation stroke could reach about 2 mm for graphene/CNT actuator in the ambient condition.[21] They have also demonstrated that, through hybridizing RGO and Ag nanoparticles, the electrochemical stability of the Ag-based electrochemical actuators was significantly improved.[23] Besides the CNT as well as nanoparticles mentioned above, electrochemical active materials such as conducting polymers (CPs) were also employed as spacers to obstacle the restacking of graphene or GO sheets.[24-29] Although earlier works have pointed out that CPs exhibited poor stability during the charge/discharge process due to the configuration change, recent work reported by Wei *et al.* have proved that PANI-GO nanocomposites electrodes displayed excellent electrochemical stability over thousands of consecutive cycles due to the synergistic effect of PANI nanowire array and GO sheets.[24] Consequently, the enhancements in actuation stroke, stress generation, and electromechanical stability are expected when graphene/CPs composite is utilized as actuator electrode.

In this work, PANI was used as an interlayer spacer to fabricate *r*-GO/PANI nanocomposite electrode due to its high specific capacitance, low cost, and facial fabrication procedure. PANI nanoparticles were directly decorated onto the *r*-GO sheets surface through in situ chemical polymerization in the presence of aniline monomer, and vacuum-assisted filtration method was employed to fabricate macroscopic free-standing *r*-GO/PANI hybrid electrode. As expected, the presence of PANI nanoparticles could effectively inhibit the restacking of graphene sheets, and then facilitate the ions migration and accumulation in the electrode layers. Acid cross-linked PVA based gel (H_2SO_4-PVA gel) was selected as electrolyte layer due to its high ionic conductivity.[30, 31] Actuation tests indicated that, the actuation could be stimulated by an extra low voltage (0.1 V), which is lower than other graphene-based air working ionic actuators reported in literature [21-23] Under a 0.5 V, 0.01 Hz square wave voltage, the bending displacement of the actuator could reach 4.300 mm, corresponding to the strain of 0.327%, larger than that of other graphene based air working actuators driven at higher voltage.[21, 23] We attribute the large actuation stroke of *r*-GO/PANI actuator to the synergistic effect of electric double-layer capacitor (EDLC) behaviour of *r*-GO component and pseudocapacitance of PANI component. Our study will guide the design and preparation of nanostructured carbon materials based ionic actuators with high actuation stroke, large generated stress and long-term durability at low driving voltages.

Experimental section

Preparation of *r*-GO and *r*-GO/PANI nanocomposite film electrodes. GO was synthesized from purified natural graphite by Hummers method according to previous work.[32] For the GO reduction, hydroiodic acid (HI) was used referred to Cheng's work.[15] Specifically, 100 ml GO solution (with concentration of 1 mg/ml) was firstly heated to 95 ± 5 ℃, then 10 ml HI was added and vigorously stirred for 20 min, after which the mixture was stirred for 12 h under room temperature. The obtained *r*-GO dispersion was washed by centrifugation using deionized water (DI H_2O) and ethanol to remove the residue I^+ and I_2, and finally dispersed in ethanol with a concentration of 0.6 mg/ml. The *r*-GO/PANI nanocomposite was synthesized by in situ polymerization in the presence of *r*-GO and aniline monomer.[24] In a typical procedure, 50 ml *r*-GO dispersion was added into 200 ml 1 M HCl solution, and 95 mg aniline monomer was added into the solution and stirred for 1 h under an ice bath to form a uniform mixture. After that, 165 mg oxidant, $(NH_4)_2S_2O_8$ (APS) was added into the above solution, and the mixture was stirred for another 24 h in the ice bath. The final *r*-GO/PANI precipitate was obtained and washed by centrifugation using DI H_2O, ethanol and 1 M HCl. The final dispersion was diluted to 0.6 mg/ml in DI H_2O. To prepare *r*-GO/PANI nanocomposites with different weight ratios, the aniline monomer with weight 47 mg and 190 mg, APS 82 mg and 330 mg, were utilized respectively. The element analysis (EA) was carried out by using a Flash EA1112 (Thermo Electron SPA) to measure the weight ratio of PANI in the nanocomposites. According to the results, the weight ratio of PANI was 50 wt %, 60 wt % and 80 wt% for *r*-GO/PANI (50/50), *r*-GO/PANI (40/60) and *r*-GO/PANI (20/80), respectively. The *r*-GO/PANI nanocomposite used for characterization is the one with 60 wt % PANI unless otherwise stated. The PANI sample was synthesized chemically at 0.15 M aniline *via* the similar procedure. The *r*-GO and *r*-GO/PANI films were prepared by vacuum filtrating 10 ml dispersion through polytetrafluoroethylene (PTFE) and cellulose membranes (47 mm in diameter, 0.22 μm pore size), respectively. After air drying, the resulting films were peeled off from the membranes. For the PANI electrode preparation, a mixture containing 85 wt % PANI powder, 10 wt % conducting carbon black and 5 wt % PTFE (used as a binder) was well mixed and pressed into a film.

Preparation of electrolyte layers. For the electrolyte preparation, 1 g PVA was dissolved in 10 ml DI H_2O, and 1 g concentrated H_2SO_4 was added. The mixture was vigorously stirred under ~85℃ for 1 h to obtain a uniform transparent solution.[31] To obtain the electrolyte layer, 1.5 ml H_2SO_4-PVA solution was cast into a PTFE mold with size of 3 × 3 cm and

dried at 40 ℃ for 4 h.

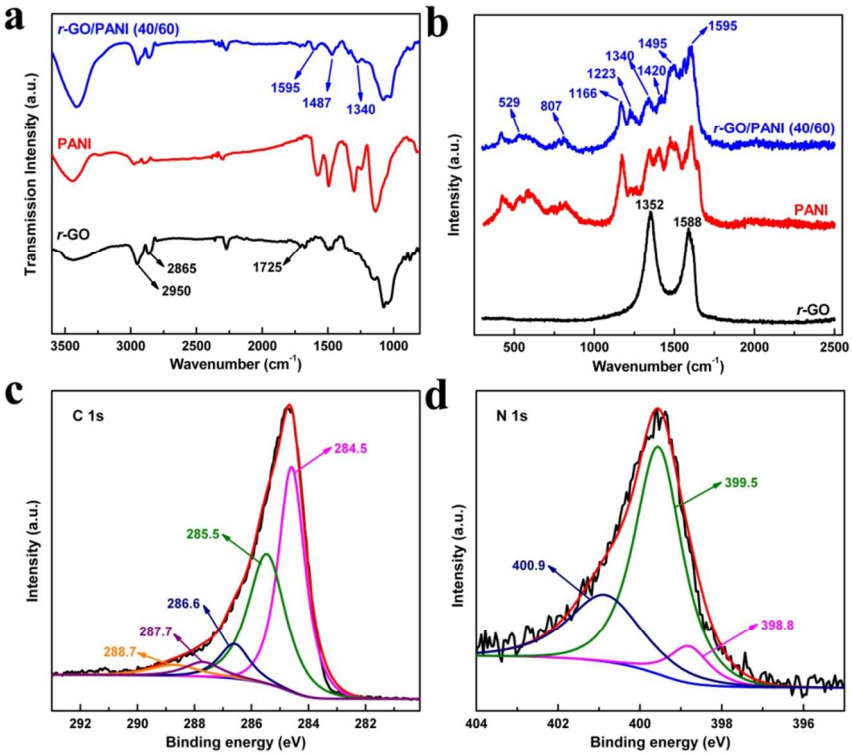

Figure 1 (a, b) FTIR and Raman spectra of pristine *r*-GO, PANI and *r*-GO/PANI nanocomposite; (c, d) C1 s and N1 s spectra of *r*-GO/PANI, respectively.

Assembly of the sandwiched actuators. The half-dried H_2SO_4-PVA gel was peeled off from the PTFE mold and two pieces of as-prepared electrode films were pasted on the two sides of the gel and pressed under 0.7 MPa for 15 min at 40 ℃. After that, the assembled actuators were aged under room temperature in air for at least 1 day to evaporate the excess H_2O in the electrolyte layer, until no weight loss was observed. The final membrane was cut into strips with size of 2 × 25 mm for actuation performance tests.

Materials characterization and actuation performance tests. The morphology of the samples was studied by Scanning Electron Microscope (SEM, HITACHI S-4800) and Transmittance Electron Microscope (TEM, Tecnai G2 F20 U-TWIN). Fourier transform infrared (FTIR) spectroscopy (Spectrum One), Raman spectroscope (using the 632.8 nm line of a He-Ne laser, equipped with a Linkam cooling cell), X-ray photoelectron spectroscopy (XPS, ESCALAB250Xi), and X-ray diffraction (XRD, Rigaku D/max-2500) were used to examine the materials microstructure. The Brunauer-Emmett-Teller (BET) surface area was measured by using a TriStar II 3020 analyzer. Electrochemical measurements were carried out on an EG&G Princeton Applied Research VMP3 workstation with two symmetrical electrodes and H_2SO_4-PVA gel as electrolyte layers. The EIS measurements were carried out at 0 V by imposing a sinusoidal perturbation of 10 mV in the frequency range from 10 mHz to 100 kHz. A dynamic mechanical analyzer (TA, DMA Q800) were employed to evaluate the mechanical properties of the resulting films. The films were cut into strips with width of 2 mm, and the gauge length was controlled to be 10.0 ± 0.5 mm. The static tensile tests were conducted in displacement ramp mode with a pre-strain 0.01% and a ramp rate 20 μm/min. For actuation performances test, electrical power was supplied by a Tektronix arbitrary function generator (AFG3011), and the bending displacements were measured using a Keyence LK-G5001 laser displacement sensor, the vertical distance of recorded point was 18 mm far from the fixed end.

Results and discussion

The structures of the electrode materials were characterized by FTIR spectra, Raman spectra and XPS analysis. In the FTIR spectrum of *r*-GO (in Figure 1a), absorption bands at 2950 and 2865 cm^{-1} are assigned to the C-H, $(C-H)_n$ stretching vibrations. The peak around 1725 cm^{-1} is originated from the stretching vibrations of C=O in COOH functional groups, indicating the partial chemical reduction of carboxyl groups. The presence of residual functional groups would act as nucleation sites for the formation of PANI nanoparticles during the polymerization process.[24] Similar to that of PANI, the peaks at 1595, 1487 and 1340 cm^{-1} appeared in *r*-GO/PANI spectrum are assigned to the C=C stretching vibration of quinonoid ring, benzenoid ring and C-N vibration of PANI, respectively.[26] Raman spectrum of *r*-GO sample in Figure 1b displays two peaks at 1352 (D band) and 1588 cm^{-1} (G band) respectively, which correspond to the *K*-point phonons of A_{1g} symmetry and the vibration of sp^2 hybridized carbon (E_{2g} phonons).[27] In the spectrum of *r*-GO/PANI sample, several new Raman peaks are detected, in which the peaks at 529 and 807 cm^{-1} are assigned to the out-of-plane C-H deformation and C-H bending of the quinonoid ring, respectively.[33] The peaks at 1495 and 1595 cm^{-1} are originated from the C=N and C=C stretching in the quinonoid ring, respectively. Other peaks at 1166, 1223, 1340 and 1420 cm^{-1} are attributed to C-H bending of

quinonoid ring, C-N vibration of quinonoid and benzenoid rings, stretching vibration of C-N^+•, C=N stretching of the quinonoid

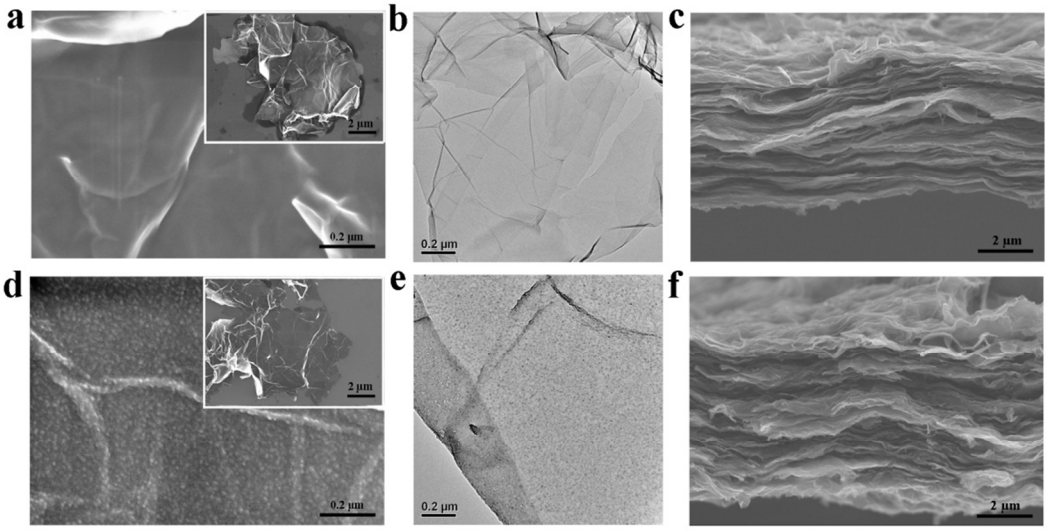

Figure 2 SEM and TEM characterization of *r*-GO sheets (a, b) and *r*-GO/PANI (40/60) hybrid sheets (d, e), insets are the overall morphology of the sheets; (c, f) cross-sectional view of free-standing *r*-GO and *r*-GO/PANI films.

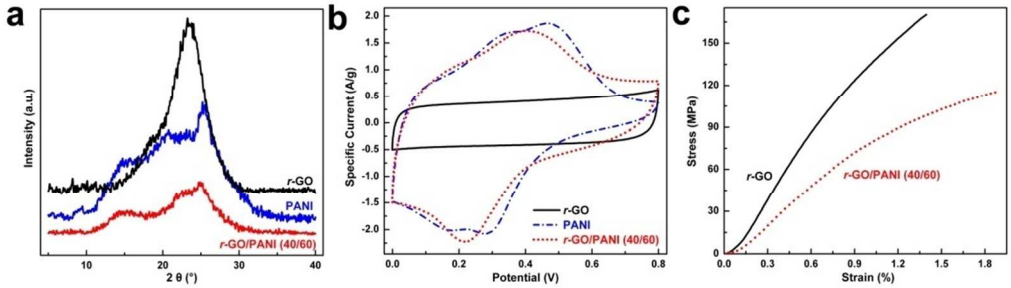

Figure 3 (a) XRD characterization; (b) CV curves at 10 mV/s scanning speed of pristine *r*-GO, PANI and *r*-GO/PANI; (c) typical stress-strain curves of pristine *r*-GO and *r*-GO/PANI nanocomposite.

ring, respectively. The presence of C-N^+• stretching vibration mode implies the PANI was doped in the nanocomposite.[34, 35] XPS characterization was used to detect the electronic structure of carbon based materials. For *r*-GO/PANI nanocomposite, the C 1s spectrum could be mainly deconvoluted into five Gaussian peaks as shown in Figure 1c, which are corresponding to C=C bond (284.5 eV), C-N bond (285.5 eV), residual C-O (286.6 eV), C=O (287.7 eV) and O-C=O (288.7 eV) functional groups, respectively. The N1s spectrum of the *r*-GO/PANI sample (in Figure 1d) shows three different electronic states existed in the N 1s spectrum: quinoid amine (398.8 eV), benzenoid amine (399.5 eV), and nitrogen cationic radical (N^+•) with binding energy of 400.9 eV.[36, 37] The relatively high fraction of N^+• in the N 1s core-level spectrum of nanocomposite samples indicated a relatively high doping level of PANI, which would be beneficial for the electrochemical properties once used as electrodes.[36, 37] From the XPS, FTIR and Raman results, we conclude that PANI was successfully attached onto the *r*-GO surface through dilute polymerization of aniline monomer.

Figure 2 shows the SEM and TEM characterization of the morphology and structure of *r*-GO, *r*-GO/PANI sheets, and its macroscopic *r*-GO, and *r*-GO/PANI papers. The *r*-GO sheets with lateral size of several micrometers exhibit a typical crumpled and layer-like structure (Figure 2a and 2b). As stated in earlier work, the *r*-GO sheets would act as excellent heterogeneous nucleation substrates for the polymerization of aniline polymer.[24-26] Figure 2d and 2e show that numerous PANI nanoparticles with size around 20 nm are uniformly decorated onto the surface of graphene sheets in *r*-GO/PANI sample. The overall morphology of the *r*-GO sheets was not affected by the presence of PANI nanoparticles, as shown in the inset of Figure 2a and 2d. Since the homogenous growth of PANI was effectively restricted in the solution, there is no apparent bulk PANI material observed from SEM and TEM images. We speculate that the presence of PANI nanoparticles onto the graphene sheets surface would hinder the stacking of *r*-GO sheets during the film formation process. We will discuss it later.

By using *r*-GO and *r*-GO/PANI sheets as building blocks, free-standing films were fabricated through vacuum assisted filtration method as reported in our previous work.[32] Figure 2c and 2f show that both *r*-GO and *r*-GO/PANI sheets could self-assemble into a layered structure. As expected, the *r*-GO/PANI film exhibits relatively loosely stacked morphology compared with the densely packed *r*-GO film. To quantitatively elucidate the influence of PANI nanoparticles on the microstructure of *r*-GO sheets, XRD characterization was carried out and the results are given in Figure 3a. The *r*-GO sheets exhibit an intense, sharp reflection peak at $2\theta = 23.24^\circ$ (assigned to (001) reflection peak), which is correlated to an interlayer spacing of 0.38 nm.[15] Neat PANI sample exhibits several broad reflection peaks around $2\theta = 15.5^\circ$,

20.7˚ and 25.2˚, which are the characteristic Bragg diffraction peaks of PANI.[38] In the case of *r*-GO/PANI sample, only the

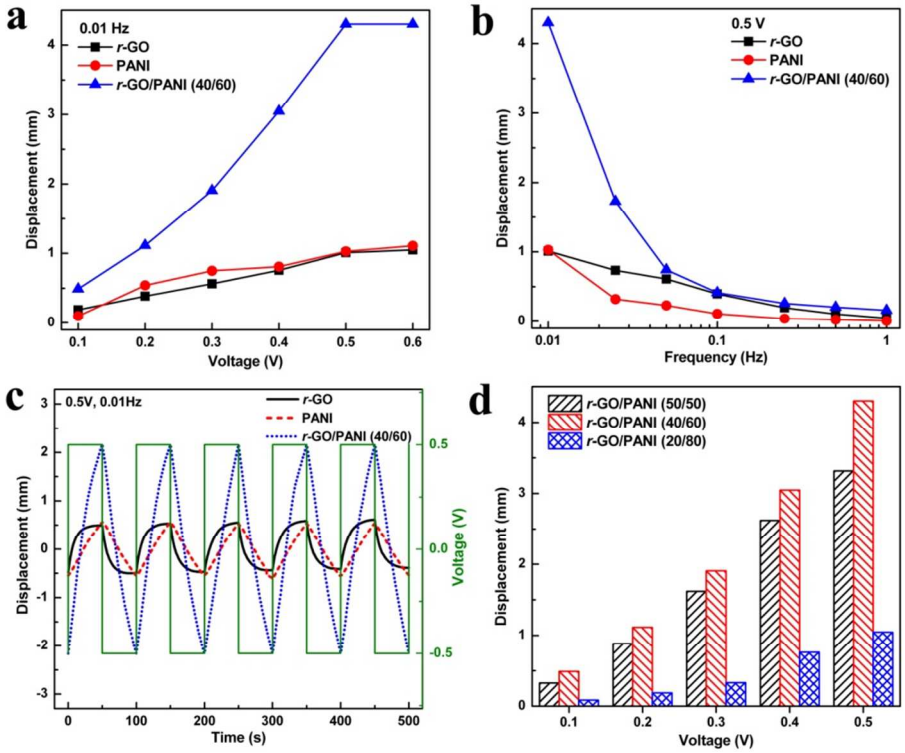

Figure 4 (a) Actuation displacements of different actuators under various driving voltage with 0.01 Hz frequency; (b) voltage-frequency-dependant actuation performances of the actuators under 0.5 V driving voltage; (c) cyclic actuation curves for *r*-GO, PANI and *r*-GO/PANI actuators under 0.5 V, 0.01 Hz square wave voltage; (d) actuation displacements of *r*-GO/PANI actuators with different PANI content under various driving voltage with 0.01 Hz frequency.

characteristic PANI reflection peaks at 2θ around 15˚ and 20-30˚ are observed. The disappearance of the reflection peak of *r*-GO sheets is attributed to the adsorption and intercalation of PANI nanoparticles, as supported by TEM and SEM characterization shown in Figure 2. The loosely packed feature of graphene sheets endows *r*-GO/PANI nanocomposite film with additional specific surface area comparing with that of the compact *r*-GO film (*r*-GO sample 3.7 m^2/g and *r*-GO/PANI sample 12.3 m^2/g). Consequently, the increment in the ionic transportation channels is expected, and would benefit the ions migration during the electrochemical charging and discharging process.

Figure 3b shows electrochemical properties of the *r*-GO, PANI and *r*-GO/PANI nanocomposite examined by cyclic voltammetry (CV) with potential window from 0 to 0.8 V and scan speed of 10 mV/s. The specific capacitance (*C*) of the electrode materials can be calculated according to Equation 1:

$$C = \int \frac{IdV}{vmV} \qquad \text{Equation 1}$$

where *I*, *v*, *V* is the charge-discharge current, potential scan speed, voltage range, respectively, *m* is the mass of the electrode. An approximate rectangular shape of CV curve of the *r*-GO electrode shown in Figure 3b indicates a typical EDLC behaviour, and the derived specific capacitance value is 79 F/g, which is close to the value reported by Chen *et al.*[39] As for PANI electrode, two couples of redox peaks are observed in the CV curve with specific capacitance 208 F/g, corresponding to two redox transitions of PANI (*i.e.*, leucoemeraldine/emeraldine transition and emeraldine/pernigraniline transition).[40] Compared with PANI, the peak positions of two redox components in the *r*-GO/PANI nanocomposite electrode are very close to each other and nearly merge into one peak, and similar phenomenon was also observed in CNT/PANI nanocomposite system.[31] The derived capacitance for *r*-GO/PANI is 207 F/g, higher than the theoretical value based on the weight ratio of *r*-GO /PANI nanocomposite (79 × 40 wt % + 208 × 60 wt % = 156 F/g). The enhancement in specific capacitance for nanocomposite electrode comes from the synergistic effect of *r*-GO sheets and PANI nanoparticles. The loosely packed *r*-GO/PANI electrodes exhibit a relatively larger rectangular area in CV curve (Figure 3b), confirming an increase in double-layer capacitance.[40] Besides that, the presence of PANI component in composite electrodes also contributes additional pseudocapacitance in electrochemical properties.

Not only the electrochemical property but also the mechanical property is an important factor to define the actuator performances. Figure 3c shows the typical tensile mechanical properties of *r*-GO and *r*-GO/PANI films. For neat *r*-GO film, tensile modulus and strength of 17.3±0.4 GPa and 154.9±11.9 MPa could be obtained. Because of the increased interlayer spacing and loosely stacked *r*-GO sheets, the modulus and strength decrease to 9.8±0.2 GPa and 115.2±5.0 MPa respectively for *r*-GO/PANI nanocomposite. However, it should be noted that, the tensile mechanical properties of composite are still higher than the existed electrode materials, such as CNT based Bucky gel (modulus is 0.2 GPa) and PANI film (modulus is 0.4 GPa).[13, 41] Eventually, large actuation stroke and high stress generation

are expected for the *r*-GO/PANI nanocomposite based actuator because of large electrochemical capacitance and good mechanical properties.

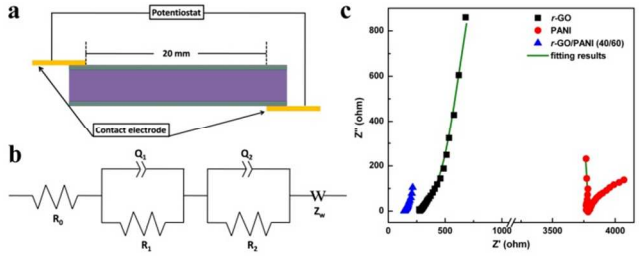

Figure 5 (a) Illustration for impedance characterization; (b) equivalent circuit model of the actuators; (C) Nyquist plots of the actuators.

The ionic-type actuators were constructed by sandwiched H_2SO_4-PVA gel with two pieces of electrode films, and the cross-sectional views of the actuators in Figure S1 indicate that the electrode and electrolyte layers were combined together tightly. The actuation strain (ε) could be quantitatively calculated using Equation 2, in which d stands for thickness of the actuator, L is the length from the fixed end to the measure point, and δ represents the actuation displacement from the initial position to peak position.

$$\varepsilon = \frac{2d\delta}{L^2+\delta^2} \qquad \text{Equation 2}$$

In this work, the values for d and L were controlled to be about 250 μm and 18 mm, respectively.

At a given frequency, the actuation strokes of ionic actuators strongly depend on the amplitudes of driving voltage, and it is desirable to stimulate the actuator under relatively low driving voltage.[8, 42] Recently, Kim *et al* have demonstrated that, by employing self-assembled sulphonated block copolymers and ionic liquids as electrolyte, the SWCNT actuator could work at sub-1-V conditions in air.[42] Herein, H_2SO_4-PVA gel is utilized as electrolyte due to its high ionic conductivity and low-cost. [30, 31] The actuation performances of the actuators were firstly investigated by applying alternating square wave voltages with various amplitudes. As shown in Figure 4a, the displacements increase with the driving potential for all actuators. More interestingly, the actuation could be triggered under an extremely low driving voltage (0.1 V), which is about one magnitude lower than that used for graphene based ionic actuators reported in reference.[21-23] Under a 0.1 V, 0.01 Hz square voltage, the peak-to-peak displacements of the *r*-GO, PANI and *r*-GO/PANI electrodes based actuators are 0.190, 0.100 and 0.490 mm, corresponding to the strain of 0.015%, 0.008% and 0.038% respectively. It can also be seen that, the deformations plateau until the voltage exceeds 0.5 V. The deformations increase to 1.010, 1.030, and 4.300 mm for *r*-GO, PANI and *r*-GO/PANI actuators at 0.5 V, while the value is 1.050, 1.110, and 4.300 mm at 0.6 V, respectively. For *r*-GO actuator, the deformation saturation should relate to the densely stacking nature of the sheets, which would block further ions transportation greatly. And for PANI and *r*-GO/PANI actuators, as seen from the CV curves shown in Figure 3b, the redox reaction happens around 0.5 V, which means more ions would be transferred and accumulated at 0.5 V; further increase the driving voltage, there will be no significantly increase in ions accumulation, and then no more bending deformation of the actuators. When the driving voltage exceeds 0.8 V, the actuation performance would be deteriorated due to the overoxidation and instability of the PANI components.

The voltage-frequency-dependant actuation performances of the actuators were explored in Figure 4b. Under a given driving voltage, the actuation stroke increases with the decrement of applied frequency. The frequency-dependent actuation strokes are attributed to variation in ions migration and accumulation, where more ions would be transported to the electrode layer at lower frequency and lead to apparent deformation of actuators. At a 0.5 V driven voltage, the bending deformation of the *r*-GO, PANI and *r*-GO/PANI actuators is 1.010, 1.030, and 4.300 mm at 0.01 Hz, corresponding to the strain of 0.077%, 0.079% and 0.327%, respectively. Figure 4c shows the cyclic bending curves for actuators under a 0.5 V, 0.01 Hz square wave voltage. For *r*-GO based actuator, the densely stacking feature severely restricts the ions migration in the electrode layers, and then the ions accumulation saturation would lead to the displacement equilibration. Different from the *r*-GO actuator, no displacement plateau region is observed for PANI and *r*-GO/PANI actuators, which could be related to the redox reaction of the PANI components. Digital pictures showing the forth and back bending deformation of *r*-GO/PANI based actuator under a 0.5 V, 0.01 Hz voltage are given in Figure S2.

To investigate the effect of PANI content on the actuation performance, *r*-GO/PANI nanocomposites with different amounts of PANI were prepared, the weight ratio of PANI was about 50 wt %, 60 wt % and 80 wt % for *r*-GO/PANI (50/50), *r*-GO/PANI (40/60), and *r*-GO/PANI (20/80), respectively, and the capacitance was measured to be 170, 207 and 106 F/g. This result indicates that, the introduction of PANI could improve the electrochemical performance of *r*-GO, and the optimal content of PANI is 60 wt %; further increase PANI content would lead to the capacitance decrease because of the nanoparticles morphology disappearance and densely coverage on the *r*-GO sheets as shown in Figure S3. Figure 4d presents the actuation performances under various voltages at 0.01 Hz. According to the results, upon increasing the weight ratio of PANI, the deformation of *r*-GO/PANI actuator increases remarkably. The displacement of the *r*-GO/PANI (50/50) reaches 3.314 mm and achieves the maximum (4.300 mm) for *r*-GO/PANI (40/60), then decreases sharply to 1.046 mm when the mass ratio of PANI is 80 wt %. It can be deduced that, the bending deformation shows the same trend as the capacitance, and *r*-GO/PANI nanocomposite with 60 wt % PANI shows the best actuation performance under same working condition.

Electrochemical impedance spectroscopy (EIS) characterization was carried out to understand the electrochemical behaviour of the actuators as it has been proved to be a useful approach to analyze the electrochemical behaviour of the air working ionic actuators.[21, 22] The experiment set up is depicted in Figure 5a, the distances between two electrodes are controlled to be 20 mm for all actuators. Figure 5b and c show the equivalent circuit used for data analysis and the obtained Nyquist plots of the actuators. The equivalent circuit mainly contains four parts: R_0, stands for the actuator resistance that mainly due to the electrolyte layer; Q_1/R_1, represents the contact impedance between the actuator electrodes and metal electrodes; Q_2/R_2 and Z_w (the Warburg impedance), indicate the ions intercalation impedance. The fitting results

obtained using this equivalent circuit are given in Table S1. According to the fitting results, the resistance R_0 is on the level of few hundreds of Ohms; comparatively, the contact resistance R_1

Figure 6 Schematic drawing of the actuation deformation.

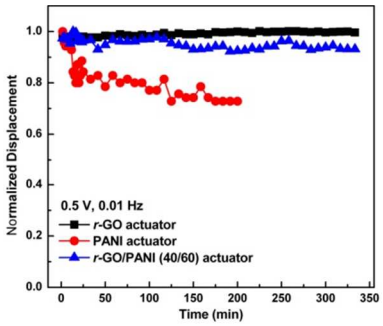

Figure 7 Cyclic stability test of *r*-GO, PANI and *r*-GO/PANI electrode based ionic actuators.

is larger than R_0, especially for PANI (3470 Ω), indicating the better electrode contact behaviour of *r*-GO (657 Ω) and *r*-GO/PANI (282 Ω). On the other hand, the diffusion ability (Z_w) for PANI and *r*-GO/PANI is relatively smaller than that for *r*-GO, but are all on the same level as given in Table S1. Additionally, after the introduction of PANI nanoparticles, R_2 of *r*-GO/PANI (1117 Ω) is significantly decreased compared with *r*-GO (6811 Ω), indicating the enhanced ions transfer ability of nanocomposite electrode. More importantly, the interfacial ions storage ability (Q_2) of *r*-GO/PANI (324.6 mF) is significantly improved compared with *r*-GO (22.4 mF) and PANI (11.4 mF), which will contribute to the capacitive behaviour of the electrode and improve the electrochemical and electromechanical properties. Based on the EIS results, we can thus deduce that, the polymerization of PANI on the *r*-GO sheets surface could significantly reduce the ions intercalation resistance and improve the ions storage ability of the electrode, which might cause actuation performance enhancement of the actuator consequently.

According to the electrochemical and actuation performances tests, the actuation mechanism of the actuators should be attributed to the EDLC behaviour of *r*-GO and pseudocapacitance of PANI, as depicted in Figure 6. When subjected to electrical stimulation, the H^+ and SO_4^{2-} ions dissociated in the gel electrolyte layer are driven to migrate and accumulate in cathode and anode respectively to keep the electric field balance. For *r*-GO electrode, the ions migration and accumulation will lead to the expansion of both the anode and cathode; however, the expansion of anode will be more significant than the cathode due to the larger SO_4^{2-} ions compared with H^+ ions, and then cause the sandwiched actuator bend toward the cathode direction under air condition. On the other hand, for PANI actuator, the ions insertion and deinsertion in polymer backbone happen during the redox reaction process to balance the charge of the system, and then lead to dimensional changes of the polymer electrodes. Specifically, the inserted SO_4^{2-} ions in PANI backbone would cause swelling of polymer chains, subsequently the anode expand, and eventually lead to a convex corresponding to the positive bias.[7, 43] After the introduction of PANI onto *r*-GO sheets surface, because of the presence of PANI nanoparticles inside gallery space, the synergistic effect of ions aggregation and redox reaction induced doping will lead to the more significant bending deformation of the actuator. The increase in specific surface area and ions transportation channels of the loosely packed *r*-GO/PANI nanocomposite film decrease the ions migration resistance and benefit ions transportation in the electrode, more ions could be inserted and accumulated in the electrodes to induce the bending deformation consequently. Besides that, the redox reaction of PANI provides excess charge transfer to allow more ions intercalation into the electrode and improve the ions storage ability, then contribute to actuation performance of the composite electrode.

In comparison with graphene and/or graphene composites based air working actuators reported in literature, the *r*-GO/PANI based actuator exhibit higher actuation strain.[21] Specifically, with the same stimulation frequency (0.01 Hz), the actuation strains for RGO and RGO/MWCNT electrode actuators were 0.248% and 0.077% respectively under 2 V potential, while the value is 0.327% for the *r*-GO/PANI actuator under a much lower voltage (0.5 V). Together with its high stiffness characteristic of nanocomposite electrode, the generated stress of the *r*-GO/PANI electrode would reach about 30 MPa, ten times higher than that for the existed ionic actuator electrode, such as Bucky gel electrode materials (about 3 MPa).[13]

The long-term stability of *r*-GO and *r*-GO/PANI actuators were investigated under 0.5 V, 0.01 Hz square wave potential as shown in Figure 7. During the cyclic actuation process, the *r*-GO electrode based actuator exhibited a quite stable working performance without any apparent decrease, implying the excellent durability of *r*-GO electrode and stable ions conductivity of the H_2SO_4-PVA gel electrolyte in air condition under long-term actuation. In comparison, PANI actuator showed a dramatic displacement decrease about 30% due to the swelling and shrinkage caused degradation of the electrode material. In contrast to the poor durability of PANI actuator, after 200 consecutive actuation cycles, the *r*-GO/PANI actuator remained ~92% of its initial displacement. The improved durability under long-term actuation of the *r*-GO/PANI actuator comes from the synergistic effect of graphene sheets and PANI nanoparticles. Graphene sheets undertake some mechanical deformation in the actuation process, which avoids the further damage of PANI component and benefits the structural stability.

Conclusions

In this work, the PANI nanoparticles were successfully decorated onto *r*-GO sheet surface through in situ polymerization in the presence of aniline monomer. The attached PANI nanoparticles effectively inhibit the restacking of *r*-GO sheets during the film preparation process and improve the electrochemical property. Electrochemical tests show that the capacitance of *r*-GO/PANI nanocomposite is increased to 207 F/g, much higher than that of *r*-GO electrodes (79 F/g). Air working ionic actuator constructed

by *r*-GO/PANI nanocomposite electrode and H_2SO_4-PVA electrolyte behave excellent low-voltage driven characteristic without trade-off actuation stroke. Specifically, under a 0.5 V square wave voltage, the bending strain could reach 0.327%. The excellent actuation performance is attributed to the synergistic effect coming from loosely packed *r*-GO sheets and redox reaction of PANI component in composite electrode, where both the ion transportation and storage ability of the electrode are significantly enhanced. Moreover, taking advantage of the excellent mechanical properties and high flexibility of graphene component, our composite actuator performs high stress generation and long-term durability.

Acknowledgment

This project was jointly supported by the National Key Basic Research Program of China (Grant Nos. 2012CB937503 and 2013CB934203) and the National Natural Science Foundation of China (Grant Nos. 51173030, 11225210 and 11222217).

Notes and references

[a] *National Center for Nanoscience and Technology, Beijing 100190, China; Fax:+86-10-8254-5586; E-mail: zhong.zhang@nanoctr.cn, Tel:+86-10-8254-5586; liulq@nanoctr.cn, Tel:+86-10-8254-5587.*
[b] *University of Chinese Academy of Science, Beijing 100049, China*

† Electronic Supplementary Information (ESI) available. See DOI: 10.1039/b000000x/

1. S. Maeda, Y. Hara, T. Sakai, R. Yoshida and S. Hashimoto, *Adv. Mater.*, 2007, **19**, 3480.
2. T. Mirfakhrai, J. Madden and R. Baughman, *Materialstoday*, 2007, **10**, 30.
3. K. Cho, J. Rosmarin and H. Asada, IEEE International Conference on Robotics and Automation, 2007, 921.
4. E. Smela, *Adv. Mater.*, 2003, **15**, 481.
5. H. Jiang, S. Kelch and A. Lendlein, *Adv. Mater.*, 2006, **18**, 1471.
6. M. Shahinpoor, Y. Bar-Cohen, J. O. Simpson and J. Smith, *Smart Mater. Struct.*, 1998, **7**, R15.
7. H. Yan, K. Tomizawa, H. Ohno and N. Toshima, *Macromol. Mater. Eng.*, 2003, **288**, 578.
8. T. Fukushima, K. Asaka, A. Kosaka and T. Aida, *Angew. Chem. Int. Ed.*, 2005, **44**, 2410.
9. K. Park, M. K. Yoon, S. Lee, J. Choi and M. Thubrikar, *Smart Mater. Struct.*, 2010, **19**, 075002.
10. R. H. Baughman, A. A. Zakhidov and W. A. de Heer, *Science*, 2002, **297**, 787.
11. Y. Zhu, S. Murali, W. Cai, X. Li, J. W. Suk, J. R. Potts and R. S. Ruoff, *Adv. Mater.*, 2010, **22**, 3906.
12. R. H. Baughman, C. Cui, A. A. Zakhidov, Z. Iqbal, J. N. Barisci, G. M. Spinks, G. G. Wallace, A. Mazzoldi, D. D. Rossi, A. G. Rinzler, O. Jashinski, S. Roth, M. Kertesz, *Science*, 1999, **284**, 1340.
13. K. Mukai, K. Asaka, T. Sugino, K. Kiyohara, I. Takeuchi, N. Terasawa, D. N. Futaba, K. Hata, T. Fukushima and T. Aida, *Adv. Mater.*, 2009, **21**, 1582.
14. D. Li, M. B. Mueller, S. Gilje, R. B. Kaner and G. G. Wallace, *Nature Nanotech.*, 2008, **3**, 101.
15. S. Pei, J. Zhao, J. Du, W. Ren and H. Cheng, *Carbon*, 2010, **48**, 4466.
16. G. W. Rogers and J. Z. Liu, *J. Am. Chem. Soc.*, 2011, **133**, 10858.
17. G. W. Rogers and J. Z. Liu, *J. Am. Chem. Soc.*, 2012, **134**, 1250.
18. X. Xie, L. Qu, C. Zhou, Y. Li, J. Zhu, H. Bai, G. Shi and L. Dai, *ACS Nano*, 2010, **4**, 6050.
19. M. Ghaffari, W. Kinsman, Y. Zhou, S. Murali, Q. Burlingame, M. Lin, R. S. Ruoff and Q. M. Zhang, *Adv. Mater.*, 2013, **25**, 6277.
20. L. Qiu, X. Yang, X. Gou, W. Yang, Z. F. Ma, G. G. Wallace and D. Li, *Chem. Eur. J.*, 2010, **16**, 10653.
21. L. Lu, J. Liu, Y. Hu, Y. Zhang, H. Randriamahazaka and W. Chen, *Adv. Mater.*, 2012, **24**, 4317.
22. G. Wu, G. H. Li, T. Lan, Y. Hu, Q. W. Li, T. Zhang and W. Chen, *J. Mater. Chem. A*, 2014, **2**, 16836.
23. L. Lu, J. Liu, Y. Hu, Y. Zhang and W. Chen, *Adv. Mater.*, 2013, **25**, 1270.
24. J. Xu, K. Wang, S. Zu, B. Han and Z. Wei, *ACS Nano*, 2010, **4**, 5019.
25. X. Yan, J. Chen, J. Yang, Q. Xue and P. Miele, *ACS Appl. Mater. Interfaces*, 2010, **2**, 2521.
26. G. Wang, W. Xing and S. Zhuo, *Electrochim. Acta*, 2012, **66**, 151.
27. F. Chen, P. Liu and Q. Zhao, *Electrochim. Acta*, 2012, **76**, 62.
28. C. Xu, J. Sun and L. Gao, *J. Mater. Chem.*, 2011, **21**, 11253.
29. J. Zhang and X. S. Zhao, *J. Phys. Chem. C*, 2012, **116**, 5420.
30. S. T. Senthilkumar, R. K. Selvan, N. Ponpandian and J. S. Melo, *RSC Adv.*, 2012, **2**, 8937.
31. C. Meng, C. Liu, L. Chen, C. Hu and S. Fan, *Nano Lett.*, 2010, **10**, 4025.
32. Y. Gao, L. Liu, S. Zu, K. Peng, D. Zhou, B. Han and Z. Zhang, *ACS Nano*, 2011, **5**, 2134.
33. H. Cong, X. Ren, P. Wang and S. Yu, *Energy Environ. Sci.*, 2013, **6**, 1185.
34. S. Ameen, M. S. Akhtar and H. S. Shin, *Sens. Actuators B*, 2012, **173**, 177.
35. S. H. Domingues, R. V. Salvatierra, M. M. Oliveirab and A. J. G. Zarbin, *Chem. Commun.*, 2011, **47**, 2592.
36. K. Zhang, L. L. Zhang, X. S. Zhao and J. Wu, *Chem. Mater.*, 2010, **22**, 1392.
37. X. Feng, R. Li, Y. Ma, R. Chen, N. Shi, Q. Fan and W. Huang, *Adv. Funct. Mater.*, 2011, **21**, 2989.
38. X. Li, H. Song, Y. Zhang, H. Wang, K. Du, H. Li, Y. Yuan and J. Huang, *Int. J. Electrochem. Sci.*, 2012, **7**, 5163.
39. Z. Q. Niu, L. Zhang, L. Liu, B. W. Zhu, H. B. Dong and X. D. Chen, *Adv. Mater.*, 2013, **25**, 4035.
40. Q. Wu, Y. Xu, Z. Yao, A. Liu and G. Shi, *ACS Nano*, 2010, **4**, 1963.
41. H. L. Wang, J. Gao, J. M. Sanainena and P. MvCarthy, *Chem. Mater.*, 2002, **14**, 2546.
42. O. Kim, T. J. Shin and M. J. Park, *Nat. Commun.*, 2013, **4**, 2208.
43. K. Kaneto, M. Kaneko, Y. Min and A. G. Macdiarmid, *Synth. Met.*, 1995, **71**, 2211.